Inertial particle dynamics in the presence of a secondary flow

Mike Garcia and Sumita Pennathur

Inertial Particle Dynamics in the Presence of a Secondary Flow

Mike Garcia and Sumita Pennathur
University of California, Santa Barbara, Department of Mechanical Engineering
Engineering Building II, Room 2355 University of California, Santa Barbara, Santa Barbara CA, 93106, USA
(Dated: April 11, 2017)

The manipulation of particles using inertial lift forces has broad implications in the separation, concentration and sorting of particles. In this work, we show that in the presence of a secondary flow, equilibrium locations of particles subject to inertial lift can be spatially varying. Using a well-defined microfabricated straight microfluidic channel with perpendicular permeate channels, we perform experiments over a range of particle sizes, inlet and outlet flow rates to highlight different focusing regimes. We show that a permeate flow can control the equilibrium location of particles, and also be used to interrogate the balance between inertial and permeate forces.

Migration and focusing of particles in finite Reynolds number flow is a phenomenon that has recently received a great deal of attention due to its ability to precisely manipulate cells and other bioparticles. Segre and Silberberg [1] experimentally documented this phenomenon in 1961, coined the "tubular pinch effect". Through their experiments in a circular pipe, they found that rigid particles migrated to an equilibrium position shaped as an annulus, with a radius of about 0.6 times the pipe radius. Influenced by these experiments, many researchers have since developed analytic and numerical models to understand the physics governing migration in such flows [2–6], and have found that hydrodynamic inertial stresses can cause particles to laterally migrate across streamlines and ultimately focus into distinct locations in the channel (largely determined by the confining geometry of the channel) [5]. The competing forces include a wall lift force, a result of interactions between the particle and a confining wall acting to push the particle away from the wall, and a shear gradient inertial force caused by the gradient of the fluid velocity profile, pushing particles toward the wall. The balance between these two forces predicts the existence of an unstable equilibrium position at the centerline, and stable equilibrium positions somewhere between the channel centerline and the wall [2].

More recently, inertial migration techniques have been exploited in microfluidic systems for applications such as the separation [7–9], concentration [10] and sorting [11] of cells and biomolecules. In these studies, researchers rely exclusively on the deterministic nature of inertial focusing combined with the incorporation of clever geometric designs to manipulate analytes of interest. Often these geometries utilize a design that can generate a secondary flow which can modify cell and particle focusing locations [12–14]. To date, no one has attempted to exploit permeate flows to dynamically control bioanalytes in inertial microscale fluidic systems, even though the incorporation of such flows is ubiquitous at the macroscale. For example, it has been documented that filtration efficiency is improved in hollow fiber membrane systems (*i.e.*, tangential flow filtration (TFF) systems) due to inertial lift forces facilitating the transport of microparticles away from membrane walls (thereby reducing fouling) [15, 16]. Predictive models of mass transfer in such filtration modules are largely based on simulating the single phase flow field in the channel and coupling the solution of the flow field to the solute mass transfer balance through the convective-diffusion equation [16]. Unfortunately, researchers often apply many simplifying assumptions with regards to the hydrodynamic inertial effects on suspended particulates that either do not account for a spatially varying axial flow rates or the influence of a secondary flow on the underlying velocity profile [17–19]. For example, Altena and Belfort [19, 20] modeled and measured inertial particle motion in a porous duct to include the effect of a constant permeate force of a single wall on a particle. The theory calculated the trajectories of particles by assuming that the inertial contribution could be superimposed with the permeate forces, the applicability of which is limited to regimes of constant permeate flow and constant axial flow rates. Under typical operation of TFF, both permeate flow and axial flow rates are spatially varying due to the fouling of membrane walls and the presence of a permeate flow, respectively.

In this work, we fabricate well-defined square cross-section microfluidic TFF devices to study resulting particle equilibrium locations due to the interplay between permeate and inertial forces. We focus on a particular case of TFF where permeate flow is spatially dependent and interrogate how these permeate forces alter the behavior of particle equilibrium streams. By observing the particle equilibrium location for a variety of particle sizes, permeate and axial flow rates, we demonstrate a novel method for measuring the spatial variation of lift forces on a particle. Finally, we demonstrate the potential for particle separations by leveraging particle inertia in the presence of a permeate flow to shift particles into size dependent equilibrium streams.

Fig. 1A shows a schematic of our microfluidic TFF device. We etch both the primary and permeate channels in silicon using typical microfabrication techniques, and anodically bond to a transparent borosilicate wafer to prevent any swelling and delamination of the permeate channels under high operating pressures (Fig. 1B). Briefly, we pattern photoresist (AZ 4620) on a 4-inch silicon wafer (100) through a single mask photolithography process, and etch the silicon using a standard Bosch process (Plasma-Therm 770 SLR) to create the high aspect ratios (AR = 20) of the permeate channels. We drill the wafer inlet and outlet vias into the silicon wafer using a 3-axis CNC drill (Flashcut), bond, and dice (ADT100) into individual dies. The primary channel is $3.2\,\mathrm{cm}$ long with a square cross sectional area of 100 x $100\,\mu\mathrm{m}$. Perpendicular to a $2.5\,\mathrm{cm}$ section of the primary channel are permeate channels of $5\,\mu\mathrm{m}$ width spaced $52.5\,\mu\mathrm{m}$ apart, with an average length of $415\,\mu\mathrm{m}$ (Fig. 1B & [21]). A two syringe pump system (Harvard Apparatus) modulates the permeate flow rate. The first pump infuses the inlet (feed) flow into the primary channel at a constant volumetric flow rate (Q_F). The second pump limits the outlet (retentate) flow rate from the primary channel by withdrawing fluid from the channel at a constant volumetric flow rate (Q_R). A global view of the device, outlining how the transverse permeate channels are arranged and how the permeate flow reaches the permeate outlets is provided in the supplemental material [21].

To perform experiments, we suspend three different fluorescent polystyrene particles (Sphereotech and FluoSpheres, 5.6, 10 and $15\,\mu\mathrm{m}$) in DI water at a concentration of 10^4 particles/mL and we add 0.5% v/v Tween 20 (Sigma-Aldrich) to reduce particle aggregation. Additionally, to measure the flow rates within the system, we conducted flow visualization experiments with $2.02\,\mu\mathrm{m}$ fluorescent polystyrene microspheres (Spherotech). We visualize all experiments with an inverted optical microscope (Olympus IX71) and mercury arc lamp illumination with the appropriate filter cubes
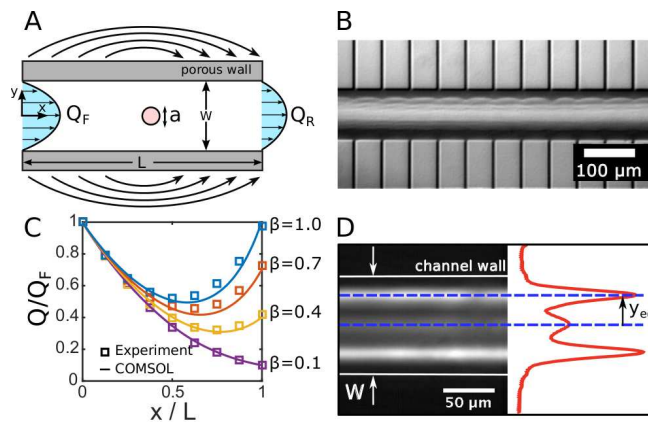
FIG. 1. (A) Schematic of TFF device with recirculating flow (B) Image of the primary channel and several perpendicular permeate channels within a microfabricated TFF device (global view of the device can be seen in [21]) (C) Non-dimensional flow rates versus channel length for varying β ($\beta = Q_R/Q_F$ = outflow/inflow). In each case, there is good agreement between COMSOL models and data. (D) (left) Long exposure image of $10\,\mu$m fluorescent polystyrene particles in a 100 x 100 μm TFF channel flowing at Re = 83. The in-plane particles equilibrate at a distance (y_{eq}) relative to the centerline. (right) Intensity distribution of the same image showing the intensity peaks used to determine (y_{eq}). Note that there are three peaks, the two larger peaks correspond to the equilibrium location of particles in-plane and the smaller peak is attributed to the out-of-plane equilibrium location of the flowing particles.

(Chroma, Inc.). To find particle equilibrium locations, we record streak images with a CCD camera (Andor Luca) by accumulating approximately 25 seconds of image data at each downstream location and post-processing using image processing software (MATLAB). Fig. 1D shows an example of a streak image and resulting post-processed data. We locate the intensity peaks through a peak finding routine and determine particle stream position at various locations along the channel.

Under typical operation, TFF devices divert a portion of the flow in the primary channel through the permeate walls, and the flow is highly dependent on the device geometry. In our geometry, the permeate resistance is comparable to the main channel resistance so flow recirculates, *i.e.*, exits the channel upstream and reenters further downstream (Fig. 1A and 1C). To understand this global flow in our system, we developed a two dimensional COMSOL model of our device (Fig. 1C) where we specified the flow rates at the inlet of the channel and at the outlet of the channel, Q_F and Q_R, respectively, and $\beta = Q_R/Q_F$ is the non-dimensional parameter quantifying the permeate flow. We determined the volumetric flow rate in the primary channel by modeling the system as an open boundary with no normal stresses, and acquired flow rates along the channel as shown in Fig. 1C. We experimentally validated this model through particle tracking velocimetry (Fig. 1C) for various values of β, and as expected, we observe a deviation from linearity of Q/Q_F due to recirculation. This design thus allows us to vary the permeate flow by simply tuning the flow rate ratio (β) which ultimately modifies the spatially varying permeate velocity and affects the migration of particles.

Fig. 2 shows a representative case ($a/W = 0.15$, Re = 138 , $\beta = 1.0$) of the particle intensity distribution along the channel length (x/L) in the presence of a spatial varying permeate flow. The channel Reynolds number is defined by $Re = \rho U W/\mu$, where ρ is the density and μ is the viscosity of water, $W = 100\,\mu$m is the width of the TFF channel, and $U = Q_F/W^2$ is the mean inlet fluid velocity in the channel. We observe three distinct regions of particle positioning: (1) The channel entrance ($0 < x/L < 0.1$), (2) the outward permeate flow region, where the permeate flow is directed into the wall, and (3) the inward permeate flow region where the permeate flow is directed into the channel. At the entrance of the channel (1), the particles enter randomly dispersed since neither the inertial nor permeate forces have had significant time to influence the particles. This stage is characterized by poor focusing quality, as the particle intensity distribution has no clear peaks. Within the outward permeate flow region (2), the permeate flow out of the primary channel shifts the equilibrium positions of the in plane particles closer to the walls and simultaneously destabilizes the out-of-plane equilibrium positions. As a consequence, the two stable in-plane equilibrium locations contain the majority of the particles. Additionally, in this region the equilibrium locations of the particles are independent of β and channel location (x/L) (Fig. 2C), since the permeate flow at least in the first third of the channel is also nearly independent of β and x/L (Fig. 1C). The inward permeate flow region (3), beginning where the permeate flow is directed into the channel and ending at the outlet of the channel ($x/L = 1$), is the region where equilibrium locations along the permeate wall move towards the centerline, and are spatially-varying throughout the remaining length of channel. This is contrasted by the case of flow in a straight channel (SC) with no permeate
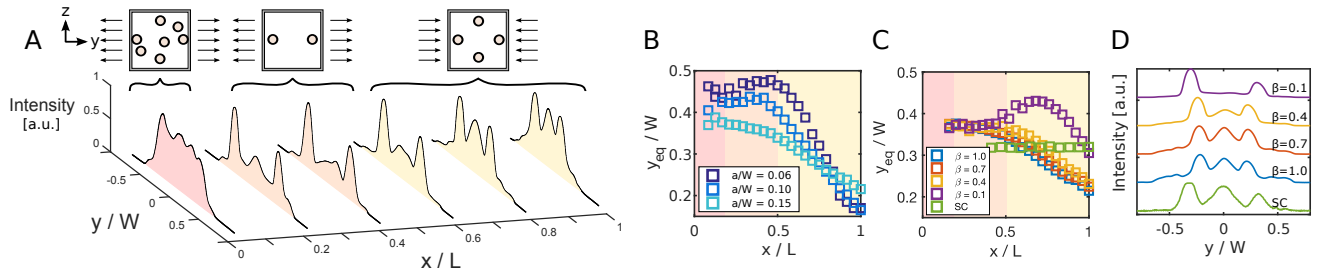
FIG. 2. Experimental particle equilibrium locations in a TFF channel. (A) One experiment showing the distribution of particles along the length of the channel (x/L) and (top) a corresponding schematic illustrating the influence of permeate flow direction on cross-sectional distribution of particles. At the entrance (left), the particles are dispersed and unfocused. In the outward permeate flow region, the particles are moving towards the wall, and so the equilibrium position is closer to the wall, and the out-of-plane equilibrium positions are unstable. In the inward permeate flow region, the equilibrium position shifts away from the wall, due to the fluid from the permeate channels flowing into the main channel, and the out-of-plane equilibrium positions regain stability. (B) Streamwise equilibrium positions for the three different particle sizes, all at a Reynolds number of 138 and a β of 1.0. (C) Experiments showing the effect of β at a Re of 138 and a/W of 0.15. This graph also superimposes results from a straight channel device (SC) where the equilibrium position is constant throughout the channel. (D) Particle intensity distributions at the end of the channel $(x/L = 1)$ for different β and a Re = 138. Here we see that as β decreases the out-of-plane equilibrium point disappears because more flow is diverted towards the wall, even at the end of the channel.

channels (Fig. 2C, green), where the equilibrium positions are constant throughout the channel. Furthermore, the out of plane equilibrium positions become more prominent as x/L increases. This is because the inward permeate forces act to stabilize these positions, and since this occurs over finite time the repopulation of particles into the out-of-plane equilibrium positions transpires over some finite distance. Decreasing β shifts the location of the beginning of this region further downstream (this location being the extremum point of the lines in Fig. 1C) and allows less distance for the repopulation of the stable equilibrium to occur. This is evidenced by (Fig. 2D) where the prominence of the out of plane equilibrium decreases with decreasing β.

The migration of equilibrium position in the third region is a direct result of the varying permeate flow acting away from the wall. To understand in more detail how permeate flow affects this migration, we examine the particle trajectories in region 3 (inward flowing permeate). We define transverse migration velocity as $U_m = dy_{eq}/dx \cdot dx/dt$, and where dy_{eq}/dx is calculated by using a linear fit of the measured trajectories (Fig. 2B and C), and the timescale dt is found by relating $U_{outlet} = dx/dt$ to the outlet stream-wise velocity $U_{outlet} = \beta Q_F/W^2$. Resulting migration velocities are shown to scale linearly with an effective Reynolds number $Re\beta$ (Fig. 3), suggesting that the migration we observe is largely a viscous phenomenon, unlike inertial migration (scaled as U^2 [22]). Although this migration is at least an order of magnitude slower than inertial migration, it is shown in Fig. 4A & B that the resulting equilibrium positions still depend on particle size. If viscous forces were the only force to balance the particle drag force, the resulting migration velocities should be independent of particle size (since both forces scale as a). We note that larger particles migrate slower, presumably because they are less susceptible to permeate forces since inertia scales as $F_L \sim a^4$. Therefore, permeate forces seem to dominate the migration of the particles, but fluid inertia is still extremely important in characterizing the equilibrium position of particles in TFF flow.

To gain further insight on the effects of permeate flow on the focusing behavior of the particles, in Figure 4C we map β to the corresponding local permeate velocity (U_P). Specifically, Fig. 4C shows the difference in equilibrium location between a TFF and a SC for the same flow rate (βQ_F) as a function of the local permeate velocity at $x/L = 1$. As the magnitude of permeate velocity increases, the particles deviate further from the SC focusing behavior. Again, smaller particles deviate further than larger particles, but interestingly, all particles seem to match the SC focusing position when the permeate velocity (U_P) is zero. Note that we experimentally find equilibrium locations for a SC $(100 \times 100\,\mu m)$ as a function of Reynolds number [23], and interpolate between these values to generate the data in Figure 4C.

The TFF system also allows us to measure the forces on particles in a manner that is not compromised at higher particle velocity. In the past, the lift forces on particles flowing in a microchannel have been difficult to measure, particularly, in a manner that can capture the spatial distribution of the forces. Most recently, K. Hood et al. [22] calculated inertial forces by tracking individual particles and calculating their lateral migration velocities. While this technique has shown excellent agreement with asymptotic theory [6], it is unclear that it would work as well for higher particles velocities, due limitations of image acquisition speeds. However, we can measure the forces on particles in a manner that is not altered by particle velocity (or equivalently Re), simply by taking advantage of a known permeate flow and how it perturbs an inertially focused equilibrium particle stream.
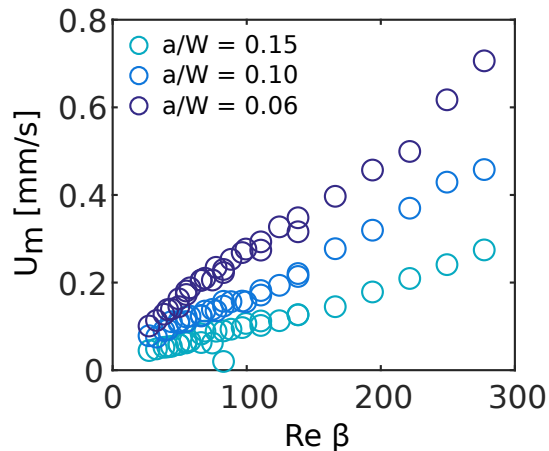
FIG. 3. Transverse migration velocities plotted against $\text{Re}\beta$. The linear results indicate that the migration is largely dominated by viscous forces, however inertial aspects are apparently important since there is a dependence on particle size (*i.e.* data does not collapse).

The lift forces on a given particle can be characterized by the lift coefficient (C_L), which is in general a function of Re and is spatially inhomogeneous [5, 24]. To calculate C_L we can compare the inertial and permeate forces at a given equilibrium location (y_{eq}) by constructing a simple model that linearly superimposes the permeate and inertial forces. The results shown in [25] show that permeate flow perturbations do not have a significant effect on axial flow profile, supporting a superposition in such a manner.

$$3\pi\mu a U_m = F_P + F_L \tag{1}$$

Furthermore, we can relate the permeate flow to a resulting transverse force using Stokes drag $F_P = 3\pi\mu a U_P$ and the inertial forces to $F_L = C_L \rho(\beta U)^2 \frac{a^4}{W^2}$ [4]. Finally, if we assume that the migration velocity is small compared to the permeate velocity at the outlet ($U_m/U_P < 0.1$) then we can derive a relationship for the inertial lift coefficient.

$$C_L = \frac{-3\pi\mu a U_P}{\rho(\beta U)^2 \frac{a^4}{W^2}} \tag{2}$$

Figures 4D and E show our experimental data recast to plot exit equilibrium locations vs. calculated lift coefficient for varying inlet Reynolds numbers and particle sizes, respectively. The measured lift coefficient values are negative near the channel walls (wall lift dominance), positive near the centerline (shear gradient lift dominance), and also show a stable equilibrium that is shifted towards the wall for both decreasing particle size and increasing Re (note that Re is based on the inlet flow rate). Therefore, inertial lift coefficients determined by our system agree not only qualitatively, but also quantitatively with previous work [5, 22]. This technique can precisely measure the distribution of force near a particle in an inertial microfluidic flow in a manner that is not compromised at higher particle velocity. This may be useful for future measurements of inertial migration at even higher Re (Re > 300).

Lastly, the TFF device is an excellent platform for particle separations because the location of the equilibrium streams is highly dependent on particle size, more so than its SC counterpart [23]. This phenomena occurs because of the disproportionate effects of permeate forces on smaller particles compared to larger (Fig. 4C). Fig. 4B demonstrates that both β and particle size determine particle equilibrium position. Specifically, Fig. 4B shows particle equilibrium locations at $x/L = 1$ as a function of particle size and β. As expected, as particle size decreases, deviation in stream location increases, and an increase in β focuses the particles closer to the centerline. While only a single Re (Re = 138) is highlighted in this figure, the trends are similar for lower Re [26]. This is believed to be a consequence of the weak dependence of y_{eq} on Re [4, 23]. These data effectively show our ability to tune the location of a particle and/or separate different particles by simply modifying β.

The work presented in this letter provides greater insight to the mechanisms influencing inertial migration and focusing in the presence of a secondary flow. We have documented a system which can not only dynamically manipulate the equilibrium location of particles, but also modify the state of equilibrium positions (stable vs. unstable). Using the TFF system we were able to measure the inertial lift forces acting on a particle by leveraging the distance an equilibrium stream is perturbed by an imposed permeate force. Finally, we demonstrated that the focusing position is
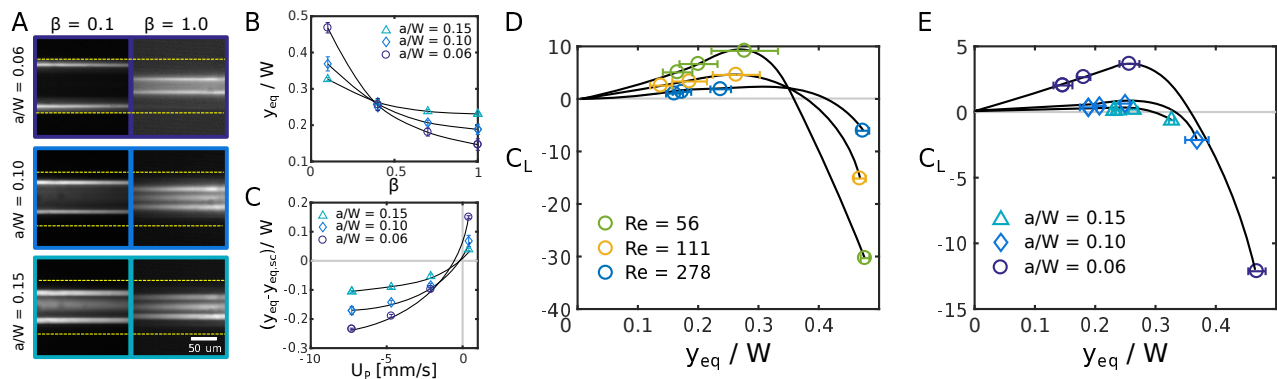
FIG. 4. (A) Grayscale streaklines of the particle focusing with three different channel sizes and two values of β.(B) Endpoint equilibrium locations vs. β for three different particle sizes ($Q_F = 50$ ml/hr at $x/L = 1$). (C) The difference between measured equilibrium locations for a TFF channel and straight channel (SC) as a function of the local permeate velocity (U_P) at the wall for $Q_F = 50$ ml/hr at $x/L = 1$. The presence of a transverse permeate flow causes inertially focused particles to deviate from their SC equilibrium location. Smaller particles are more susceptible to permeate flow as characterized by larger deviations from the SC equilibrium for a given permeate flow. The location of the TFF equilibrium returns to that of the SC in the absence of permeate flow. Measured values of the lift coefficient (C_L) on particles flowing in a TFF channel for various (D) Re = 56, 11, & 278 a/W = 0.06 and (E) particle sizes a = 5.6, 10 and 15 μm (Re = 138).

strongly dependent on particle size. This enhancement can be attributed to increased susceptibility to permeate forces for smaller particles (see Fig. 4C). In particular, the optimal flow configuration tested seems to be at $\beta = 0.1$ where we observe a 3-fold increase in the separation distance between the SC counterpart. Thus, the insight gained through this fundamental study can be applied in the design of novel separation techniques, where in-situ manipulations of particles are needed.

[1] G. Segré and A. Silberberg, "Radial Particle Displacements in Poiseuille Flow of Suspensions," Nature **189**, 209 (1961).
[2] B. P. Ho and L. G. Leal, "Inertial migration of rigid spheres in two-dimensional unidirectional flows," J. Fluid Mech. **65**, 365 (1974).
[3] J. A. Schonberg and E. J. Hinch, "Inertial migration of a sphere in Poiseuille flow," J. Fluid Mech. **203**, 517 (1989).
[4] E. S. Asmolov, "The inertial lift on a spherical particle in a plane Poiseuille flow at large channel Reynolds number," J. Fluid Mech. **381**, 63 (1999).
[5] D. Di Carlo, J. F. Edd, K. J. Humphry, H. A. Stone, and M. Toner, "Particle Segregation and Dynamics in Confined Flows," Phys. Rev. Lett. **102**, 094503 (2009).
[6] K. Hood, S. Lee, and M. Roper, "Inertial migration of a rigid sphere in three-dimensional Poiseuille flow," J. Fluid Mech. **765**, 452 (2015).
[7] A. Sarkar, H. W. Hou, A. E. Mahan, J. Han, and G. Alter, "Multiplexed Affinity-Based Separation of Proteins and Cells Using Inertial Microfluidics," Sci. Rep. **6**, 23589 (2016).
[8] J. Zhang, S. Yan, R. Sluyter, W. Li, G. Alici, and N. Nguyen, "Inertial particle separation by differential equilibrium positions in a symmetrical serpentine micro-channel," Sci. Rep. **4**, 4527 (2014).
[9] A. J. Mach and D. Di Carlo, "Continuous scalable blood filtration device using inertial microfluidics," Biotechnol. Bioeng. **107**, 302 (2010).
[10] J. M. Martel, K. C. Smith, M. Dlamini, K. Pletcher, J. Yang, M. Karabacak, D. A. Haber, R. Kapur, and M. Toner, "Continuous Flow Microfluidic Bioparticle Concentrator," Sci. Rep. **5**, 11300 (2015).
[11] S. S. Kuntaegowdanahalli, A. A. S. Bhagat, G. Kumar, and I. Papautsky, "Inertial microfluidics for continuous particle separation in spiral microchannels," Lab Chip **9**, 2973 (2009).
[12] Z. Wu, Y. Chen, M. Wang, and A. J. Chung, "Continuous inertial microparticle and blood cell separation in straight channels with local microstructures," Lab Chip **16**, 532 (2016).
[13] D. R. Gossett and D. Di Carlo, "Particle Focusing Mechanisms in Curving Confined Flows," Anal. Chem. **81**, 8459 (2009).
[14] E. Sollier, H. Amini, D. E. Go, P. A. Sandoz, K. Owsley, and D. Di Carlo, "Inertial microfluidic programming of microparticle-laden flows for solution transfer around cells and particles," Microfluid Nanofluid **19**, 53 (2015).

[15] A. Pabby, S. Rizvi, and A. Requena, eds., *Handbook of Membrane Separations*, Chemical, Pharmaceutical, Food, and Biotechnological Applications, Second Edition (CRC Press, 2015).

[16] G. Belfort, R. H. Davis, and A. L. Zydney, "The behavior of suspensions and macromolecular solutions in crossflow microfiltration," J. Membr. Sci. **96**, 1 (1994).

[17] M. Kim and A. Zydney, "Theoretical analysis of particle trajectories and sieving in a two-dimensional cross-flow filtration system," J. Membr. Sci. **281**, 666 (2006).

[18] A. M. C. van Dinther, C. G. P. H. Schroën, and R. M. Boom, "High-flux membrane separation using fluid skimming dominated convective fluid flow," J. Membr. Sci. **371**, 20 (2011).

[19] F. W. Altena and G. Belfort, "Lateral migration of spherical particles in porous flow channels: application to membrane filtration," Chem. Eng. Sci. **39**, 343 (1984).

[20] J. R. Otis, F. W. Altena, J. T. Mahar, and G. Belfort, "Measurements of single spherical particle trajectories with lateral migration in a slit with one porous wall under laminar flow conditions," Experiments in Fluids **4**, 1 (1986).

[21] See Supplemental Material at [URL] for a detailed view of the TFF channel.

[22] K. Hood, S. Kahkeshani, D. Di Carlo, and M. Roper, "Direct measurement of particle inertial migration in rectangular microchannels," Lab Chip **16**, 2840 (2016).

[23] See Supplemental Material at [URL] for particle focusing positions at various Re in a straight channel.

[24] J. Zhou and I. Papautsky, "Fundamentals of inertial focusing in microchannels," Lab Chip **13**, 1121 (2013).

[25] See Supplemental Material at [URL] for COMSOL flow simulation results.

[26] See Supplemental Material at [URL] for particle focusing positions at various Re in a TFF channel .